Nanophotonic Quantum Storage at Telecommunication Wavelength

Ioana Craiciu,[1,2] Mi Lei,[1,2] Jake Rochman,[1,2] Jonathan M. Kindem,[1,2] John G. Bartholomew,[1,2] Evan Miyazono,[1,2] Tian Zhong,[1,2,†] Neil Sinclair,[3,4] and Andrei Faraon[1,2,*]

[1] *Kavli Nanoscience Institute and Thomas J. Watson, Sr., Laboratories of Applied Physics, California Institute of Technology, Pasadena, California 91125, USA*

[2] *Institute for Quantum Information and Matter, California Institute of Technology, Pasadena, California 91125, USA*

[3] *Division of Physics, Mathematics and Astronomy, California Institute of Technology, Pasadena, California 91125, USA*

[4] *Alliance for Quantum Technologies, California Institute of Technology, Pasadena, California 91125, USA*

(Received 15 January 2019; revised manuscript received 24 June 2019; published 30 August 2019)

Quantum memories for light are important components for future long-distance quantum networks. We present on-chip quantum storage of telecommunication-band light at the single-photon level in an ensemble of erbium-167 ions in an yttrium orthosilicate photonic crystal nanobeam resonator. Storage times of up to 10 μs are demonstrated with an all-optical atomic-frequency-comb protocol in a dilution refrigerator under a magnetic field of 380 mT. We show this quantum-storage platform to have high bandwidth, high fidelity, and multimode capacity, and we outline a path toward an efficient erbium-167 quantum memory for light.

DOI: 10.1103/PhysRevApplied.12.024062

I. INTRODUCTION

Optical quantum memories can aid processes involving the transfer of quantum information via photons, with applications in long-distance quantum communication and quantum-information processing [1–5]. Rare-earth ions in crystals are a promising solid-state platform for optical quantum memories due to their long-lived optical and spin transitions that are highly coherent at cryogenic temperatures [6,7]. Among rare-earth ions, only erbium has been shown to possess highly coherent optical transitions in the telecommunication C band, which allows integration of memory systems with low-loss optical fibers and integrated silicon photonics [8].

Fixed-delay quantum storage for less than 50 ns at telecommunication wavelengths has been demonstrated in erbium-doped fibers [9], and lithium niobate waveguides [10] at efficiencies approaching 1%. The protocol used in both cases, the atomic frequency comb (AFC), requires spectrally selective optical pumping [11]. The storage efficiencies in these studies were limited in part by the lack of suitable long-lived shelving states in the erbium ions in these hosts. Moving to isotopically purified erbium-167 in an yttrium orthosilicate host (YSO) offers the prospect of long-lived shelving states in the form of hyperfine levels [12]. While optical storage has been realized in erbium-doped YSO [13–15], including efficiencies approaching 50% for storage times of 16 μs (revival-of-silenced-echo protocol [15]), quantum storage has yet to be demonstrated in this material.

In this work, we demonstrate on-chip quantum storage of telecommunication light at the single-photon level. We use a nanophotonic crystal cavity milled directly in $^{167}Er^{3+}$-doped YSO ($^{167}Er^{3+}$:YSO) for coupling to an ensemble of erbium ions and realize quantum storage using the AFC protocol [11]. The cavity increases the absorption of light by the ion ensemble, allowing on-chip implementation of the memory protocol [16]. By working in a dilution refrigerator and using permanent magnets to apply a field of 380 mT, we access a regime in which the ions have optical coherence times of approximately 150 μs and long-lived spin states to allow spectral tailoring. For a storage time of 165 ns, we achieve an efficiency of 0.2%, with lower efficiencies for longer storage times, up to 10 μs. We demonstrate storage of multiple temporal modes and measure a high fidelity of storage, exceeding the classical limit. Lastly, we identify the limits on the storage efficiency and propose ways to overcome them to achieve an efficient $^{167}Er^{3+}$:YSO quantum memory for light.

II. OVERVIEW OF THE SYSTEM

Memories using spectral tailoring such as the AFC protocol require a long-lived level within the optical-

*faraon@caltech.edu

†Present address: Institute of Molecular Engineering, University of Chicago, Chicago, Illinois 60637, USA.

ground-state manifold, where the population can be shelved. Hyperfine levels in the optical ground state in $^{167}Er^{3+}$:YSO have been shown to have long lifetimes at 1.4 K and a magnetic field of 7 T [12]. In general, these levels can be long-lived when the erbium electron spin is frozen, which occurs when $\hbar\omega_e \gg k_B T$, where ω_e is the electron Zeeman splitting [12]. In this work, we satisfy this inequality by using a moderate magnetic field of 380 mT parallel to the D_1 axis of the crystal ($\omega_e = 2\pi \times 80$ GHz) and a nanobeam temperature of approximately 400 mK (see Appendix A). The hyperfine lifetime is measured to be 29 min in the bulk crystal under the same magnetic field and cooling conditions.

Figures 1(a) and 1(b) show the nanoresonator used in this experiment. A triangular nanobeam photonic crystal cavity [17] is milled in a YSO crystal doped with isotopically purified $^{167}Er^{3+}$ (92% purity) at a nominal concentration of 50 ppm. The nanobeam is 1.5 μm wide and approximately 20 μm long. The slots in the nanobeam create a photonic crystal band gap, and the periodic pattern (lattice constant 590 nm, groove width 450 nm) is modified quadratically in the center to create a cavity mode.

Figure 1(c) shows a schematic of the optical testing setup. A fiber-coupled tunable external-cavity diode laser is used to probe the nanobeam device and implement the AFC storage protocol. One percent of the laser light is directed to a wavemeter for measurement. Another 1% of the light is picked off and sent to a locking setup, in which the laser frequency is stabilized by locking to a homebuilt fiber cavity by means of the Pound-Drever-Hall technique [18]. The remaining light is directed to the sample through two acousto-optic modulators for pulse shaping, as well as an electro-optic phase modulator to control the phase of the light and to add strong sidebands for hyperfine initialization. Neutral-density filters and polarization paddles provide attenuation and polarization control, respectively. A circulator directs light to the $^{167}Er^{3+}$:YSO crystal located inside a dilution refrigerator, thermally linked to the 25-mK stage. An aspheric lens pair focuses light from an optical fiber onto the angled coupler of the resonator. A stack of x-y-z nanopositioners is used to optimize free-space coupling. Light from the resonator is directed by the circulator onto a superconducting-nanowire single-photon detector at approximately 100 mK. Strong initialization pulses are prevented from reaching

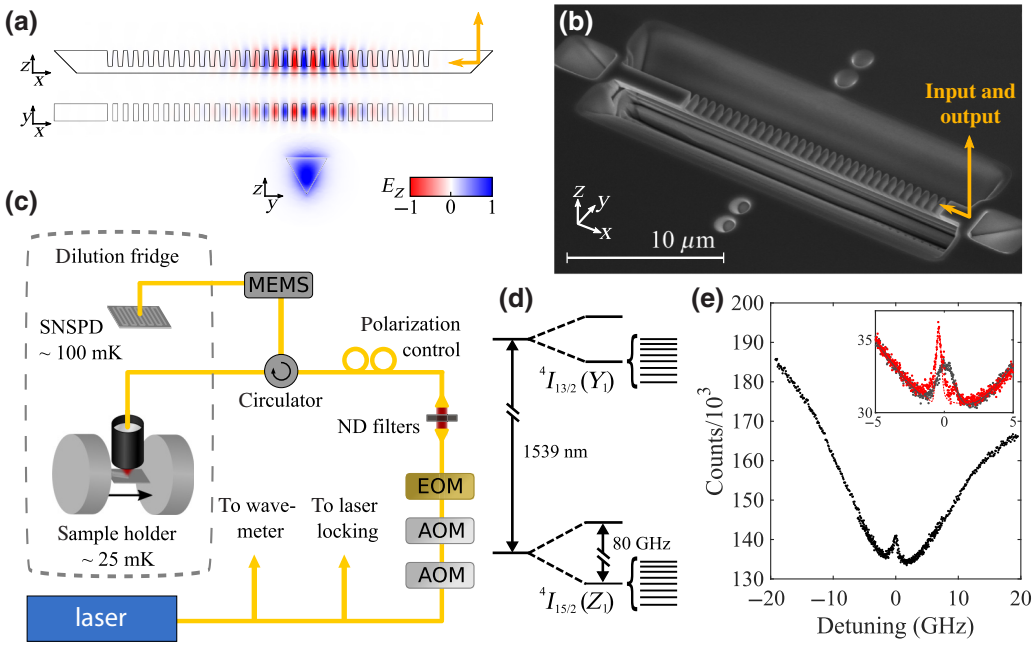

FIG. 1. (a) Finite-element-analysis simulation of the TM cavity mode in the triangular nanobeam resonator. The red-blue color gradient indicates the electric field component normal to the surface, E_z; the black outline indicates the YSO-air interface; a yellow arrow indicates coupling. (b) Scanning electron micrograph of the resonator, showing input and output coupling through a 45° slot coupler. (c) Experimental setup (details are given in the main text). (d) Energy diagram of $^{167}Er^{3+}$:YSO, showing the $^4I_{15/2} \rightarrow {}^4I_{13/2}$ optical transition for crystallographic site 2. (e) Reflection spectrum of the cavity when tuned on resonance to the 1539-nm $^{167}Er^{3+}$:YSO transition. Detuning is measured from 194 816 ± 2 GHz. The inset shows a close up of ion coupling before (black) and after (red) partial hyperfine initialization. The circles are data points, and solid black and dashed red lines are fits to theory (see the main text for details). AOM, acousto-optic modulator; EOM, electro-optic phase modulator; MEMS, microelectromechanical switch; ND, neutual density; SNSPD, superconducting-nanowire single-photon detector.

the superconducting-nanowire single-photon detector by a microelectromechanical switch. A magnetic field $\mathbf{B} =$ 380 mT is applied to the sample with use of two cylindrical permanent magnets.

Figure 1(d) shows an energy diagram of an $^{167}Er^{3+}$ ion in YSO. The ground-state and excited-state manifolds both have 16 hyperfine states ($I = 7/2$ nuclear spin, $S = 1/2$ effective electron spin), split into two sets of eight by electron Zeeman coupling to the applied magnetic field. The optical transition used in this work couples the lower eight hyperfine levels of the ground-state and excited-state manifolds. The coherence time of this optical transition is measured by the two-pulse photon-echo method [19] to be 149 ± 4 μs in the nanobeam. This provides an upper bound on the all-optical storage time. In the bulk crystal, the optical coherence time of this transition under similar cooling conditions is measured to be 759 ± 41 μs. The reduction in the coherence time as measured in the nanobeam is likely caused by a combination of higher temperature in the nanobeam during measurement and the impact of the fabrication process. At 1 K, the coherence time of ions in the bulk crystal is found to be 136 ± 9 μs. In similar nanobeam devices [20,21], focused-ion-beam milling does not significantly impact the coherence properties of ions. However, the longer bulk coherence times measured in the current work allows a higher sensitivity probe of the ions' environment. The optical coherence time does not limit the storage time achieved in this work.

Figure 1(e) shows the reflection spectrum of the nanobeam cavity, which has a measured loaded quality factor of 7×10^3. The cavity is tuned onto resonance with the 1539-nm transition of the $^{167}Er^{3+}$ ions by our freezing nitrogen gas onto the nanobeam at cryogenic temperatures [22]. The coupling of the ensemble of ions to the cavity is seen as a peak in the cavity reflection dip. The inset shows a close up of the ion-cavity coupling (in black). The ensemble cooperativity is estimated from a fit to this curve to be 0.1 (see Appendix B).

For high-efficiency storage using ions coupled to a cavity, the ensemble cooperativity should be 1 [16,23]. An increased ensemble cooperativity of 0.3 [inset in Fig. 1(e), in red], is obtained with a partial-hyperfine-initialization procedure. The width of the 1539-nm transition in $^{167}Er^{3+}$:YSO is approximately 1.5 GHz. This is broader than the true inhomogeneous linewidth of approximately 150 MHz because of the numerous closely spaced optical transitions arising from hyperfine splitting in both the ground-state manifold and the excited-state manifold [see Fig. 1(d)]. Because the ion population is distributed among the hyperfine ground states, the optical depth in the center of the 1539-nm line is lower than for an $I = 0$ isotope. Therefore, to increase the ensemble cooperativity, the ion population is first initialized into a small number of hyperfine ground states with optical transitions at the center of the inhomogeneous line. This is achieved by our sweeping the laser frequency between 350 and 820 MHz on both sides of the inhomogeneous line. At 7 T, the entire optical-ground-state population can be initialized into one hyperfine state with an efficiency of 95% by pumping on all $\Delta m = +1$ transitions or all $\Delta m = -1$ transitions [12]. At 380 mT parallel to the D_1 axis, only a partial initialization can be performed because the $\Delta m = \pm 1$ transitions are not fully spectrally resolved from the $\Delta m = 0$ transitions. The partial-initialization procedure can be improved by using larger magnetic fields or by changing the angle of the applied field.

III. ATOMIC FREQUENCY COMB STORAGE

The nanobeam device is used to demonstrate quantum optical storage using the AFC protocol [11]. In this protocol, a pulse of light that is absorbed by an atomic frequency comb with an intertooth spacing of Δ is stored for $t = 1/\Delta$. Frequency-selective optical pumping is used to create a

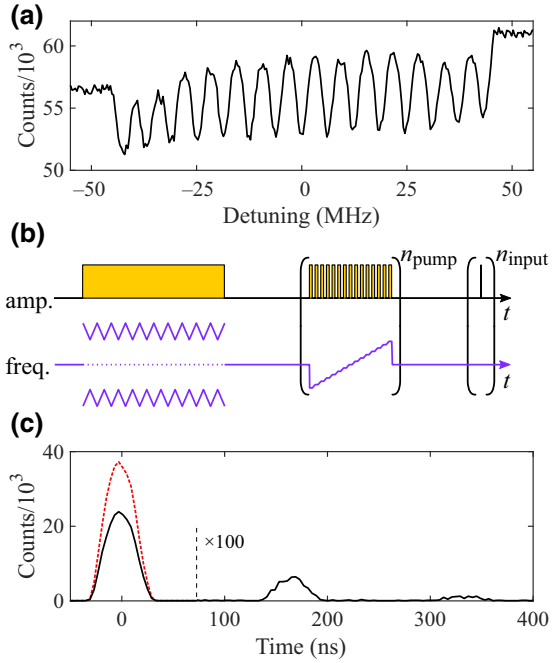

FIG. 2. AFC experiment in the nanobeam cavity. (a) A section of the resonator reflection spectrum, showing an atomic frequency comb in the center of the inhomogeneously broadened $^{167}Er^{3+}$ transition. Detuning is measured from $194\,814.2 \pm 0.1$ GHz. The apparent slope of the comb is due to its center frequency not being precisely aligned to the cavity resonance, leading to a dispersive shape. (b) AFC pulse sequence showing amplitude (yellow) and frequency (purple) modulation of the laser (pulses not to scale, see the main text for detail). (c) AFC storage: the input pulse (dashed red line) is partially absorbed by the comb; an output pulse is emitted at time $t = 1/\Delta =$ 165 ns (black line, $\times 100$). The black line also shows the partially reflected input pulse ($t = 0$) and a smaller second output pulse at $t = 330$ ns.

comb within the inhomogeneous linewidth, as shown in Fig. 2(a). Figure 2(b) shows a schematic of the protocol. First, a long pulse with strong frequency-modulated sidebands is used for partial hyperfine initialization. The next 15 pulses, repeated $n_{\text{pump}} = 20$ times, create the comb: the laser frequency is swept through 15 values, separated by $\Delta = 6.1$ MHz, to optically pump away ions and create 15 spectral transparencies. The following $n_{\text{input}} = 60$ pulses are zero-detuning weak coherent states that are stored in the frequency comb. The full experiment is repeated approximately 10^4 times. As shown in Fig. 2(c), 60-ns-wide pulses with an average photon number $\bar{n}$ of 0.60 ± 0.09 are stored for 165 ns with an efficiency of 0.2%. Despite the partial initialization, the storage efficiency is limited by the ensemble cooperativity of the device (see Appendix D).

Coherent pulses can be stored in the device for up to 10 μs, although with a lower efficiency of 10^{-5}, as shown in Fig. 3. Here, as for all storage times longer than 165 ns, we use an accumulated-AFC method [24] to create the comb. As shown in the inset in Fig. 3, weak pairs of pulses separated by $t_{\text{storage}} = 10$ μs are repeatedly sent into the cavity. The Fourier transform of each pulse pair is a frequency comb, which imprints onto the $^{167}Er^{3+}$ inhomogeneous line to create the AFC. This procedure uses laser-frequency stabilization during comb creation, which enables the creation of fine-toothed AFCs required for longer storage. For the 165-ns storage, where a coarser AFC is practical, the procedure shown in Fig. 2(b) with no laser-frequency stabilization leads to higher efficiencies by creating a more-consistent comb over the entire bandwidth. This is because the accumulated AFC has a sinc-function envelope. The storage efficiency at 10 μs is limited by residual laser-frequency jitter and by superhyperfine coupling to the yttrium ions in YSO. Superhyperfine coupling limits the narrowest spectral feature to approximately 1 MHz [25,26]. Since this exceeds the period of the comb needed for this storage time ($\Delta = 1/t_{\text{storage}} = 0.1$ MHz), the resulting AFC will have a lower contrast, leading to lower storage efficiency.

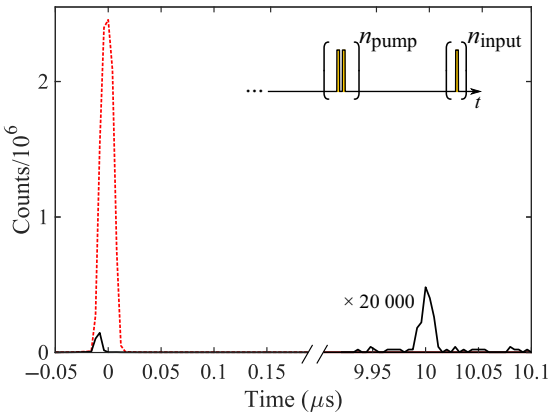

FIG. 3. AFC storage for 10 μs in the nanobeam resonator. The dashed red line shows the input pulse. The black line shows the partially reflected input pulse and the output pulse (×20 000). The reflected input pulse appears small due to detector saturation. The inset shows a schematic of the pulse sequence following hyperfine initialization. Pairs of comb-preparation pulses 10 μs apart are repeated $n_{\text{pump}} = 10\,000$ times, followed by input pulses 20 ns wide, repeated $n_{\text{input}} = 10$ times.

The AFC protocol is capable of storing multiple temporal modes [11]. Ten coherent pulses are stored in this device, as shown in Fig. 4(a). The AFC comb in Fig. 2(a) has a bandwidth of approximately 90 MHz, which can accommodate storage in multiple frequency modes [27]. An inhomogeneous linewidth of 150 MHz limits the bandwidth of storage in this system. Although there are methods to increase this linewidth [28], the bandwidth cannot be increased much further before being limited by overlapping optical transitions from other hyperfine levels.

In quantum storage protocols, the phase of the stored state must be preserved. A double AFC is used as an interferometer to characterize the coherence of the storage process [24]. Two overlapping AFCs with tooth spacing

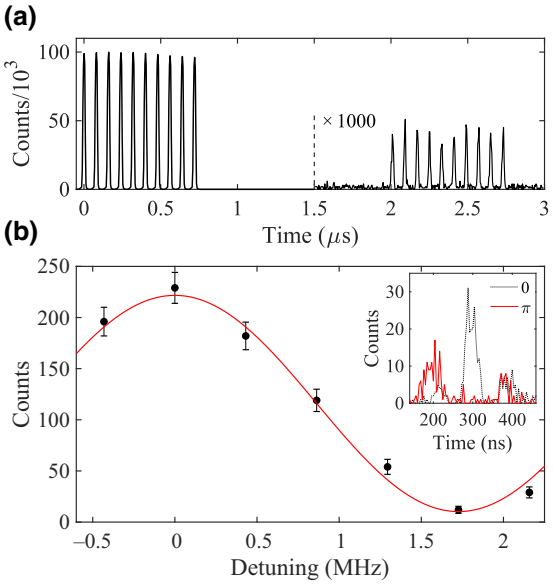

FIG. 4. Multimode and coherent storage in the nanobeam resonator. (a) Storage of multiple temporal modes: ten 20-ns-wide input pulses (reflection off cavity shown) and the corresponding ten output pulses (×1000) from a 500-kHz AFC. (b) Visibility curve acquired in a double-comb experiment, with $\Delta_1 = 5.2$ MHz, $\Delta_2 = 3.4$ MHz, and $\delta_1 = 0$ MHz. The detuning of the second comb is swept from $\delta_2 = -0.2$ MHz to $\delta_2 = 2.2$ MHz, and the intensity of the two central overlapping output pulses is measured. Black circles show the sum of counts in the overlapping pulse region with $\sqrt{N_{\text{counts}}}$ uncertainty bars. The red line shows a least-squares fit to a sinusoid. The inset shows the four output pulses (middle two overlapping) in the case of maximally constructive (dashed black line) and maximally destructive (solid red line) interference.

Δ_1 and Δ_2 and with frequency detuning δ_1 and δ_2 are created so that each input pulse is mapped to two output pulses at times $1/\Delta_1$ and $1/\Delta_2$ and with a relative phase $\phi_{\text{rel}} = 2\pi\,(\delta_2/\Delta_2 - \delta_1/\Delta_1)$ [11]. An input state encoded into two pulses, $|\psi_{\text{in}}\rangle = (1/\sqrt{2})\,(|\text{early}\rangle + |\text{late}\rangle)$, is therefore mapped to a total of four output pulses. By our appropriately selecting the time interval between the early and late input pulses, two of the four output pulses are made to overlap and either constructively or destructively interfere, depending on ϕ_{rel} [see the inset in Fig. 4(b)]. Using an input state with mean photon number $\bar{n} = 0.6 \pm 0.09$ and sweeping ϕ_{rel} via the detuning δ_2, we obtain the interference fringe shown in Fig. 4(b) (see the caption for details). The measured visibility of $(91.2 \pm 3.4)\%$ demonstrates the high degree of coherence of this on-chip storage process. The visibility is limited by the 12 counts in the total-destructive-interference case ($\delta_2 = \Delta_2/2 \rightarrow \phi_{\text{rel}} = \pi$). A dark count rate of 18.5 Hz accounts for seven of these. The remaining counts arise from imperfect cancellation of the two overlapping output pulses due to slightly different efficiencies of storage in the two AFCs. The dark-count-subtracted visibility is $(97.0 \pm 3.6)\%$.

The double-comb method is also used to estimate a lower bound for the fidelity of storing single-photon time-bin states, $F^{(n=1)}$. The fidelity of storage is measured for four input states—$|\text{early}\rangle$, $|\text{late}\rangle$,$(|\text{early}\rangle + |\text{late}\rangle)/\sqrt{2}$, and $(|\text{early}\rangle - |\text{late}\rangle)/\sqrt{2}$—with two mean photon numbers $\bar{n} = 0.30$ and $\bar{n} = 0.60$. With these values, the decoy-state method [27,29] is used to calculate a bound on the fidelity for storing single-photon states $F^{(n=1)} \geq (93.7 \pm 2.4)\%$, which exceeds the classical limit of $F = 2/3$ (details are given in Appendix C). Similarly to the visibility case discussed above, the measured fidelity is limited in part by dark counts and in part by the double-comb protocol being an imperfect interferometer. The dark-count-limited-fidelity bound is estimated to be approximately 96.5%. Although the pulses stored in this experiment are weak coherent pulses, single-photon sources [30–35] and entangled-photon sources [36,37] are available at telecommunication wavelengths, and storing photons of any frequency is enabled by quantum frequency conversion [38]. For efficient storage, the bandwidth of compatible photons is bounded by the periodicity of approximately 1 MHz and the bandwidth of approximately 100 MHz of the AFC.

IV. DISCUSSION

While the storage presented here is limited in efficiency, a nanophotonic cavity coupled to $^{167}Er^{3+}$ ions in YSO promises to be an efficient quantum storage system. The main limitations to the storage efficiency in this work are a low ensemble cooperativity of 0.3 and loss from the optical nanobeam cavity. The cooperativity can be increased using higher $^{167}Er^{3+}$ doping and better hyperfine initialization, which would require the applied magnetic field to be increased [12] or its angle to be changed. A higher-intrinsic-quality-factor resonator would serve to both increase cooperativity and decrease cavity loss. For example, with use of a YSO crystal with 200-ppm $^{167}Er^{3+}$ doping, optimal hyperfine initialization, and a resonator with an intrinsic quality factor of 2×10^6, the theoretical efficiency of the AFC quantum storage is 90% (see Appendix D for analysis). Mature silicon nanofabrication technology can be leveraged to achieve this goal by use of a silicon resonator evanescently coupled to $^{167}Er^{3+}$ ions in YSO [8,33]. With this efficiency level and a storage time of 10 μs, the device would outperform a delay line composed of standard telecommunication fiber [39], an important benchmark on the way to achieving a quantum memory suitable for scalable quantum networks.

With the optical AFC protocol alone, it will be difficult to achieve efficient storage for this duration due to superhyperfine coupling. However, the AFC spin-wave protocol, where the stored information is reversibly transferred from the optical manifold to the hyperfine manifold [11], would enable storage longer than 10 μs without the same requirements for narrow spectral features, and would also enable on-demand recall. The availability of hyperfine states with coherence times exceeding 1 s [12] makes $^{167}Er^{3+}$:YSO a promising system for spin-wave storage.

V. CONCLUSION

In conclusion, we demonstrate on-chip quantum storage of telecommunication-band light at the single-photon level. The storage has a bandwidth of approximately 90 MHz, and a storage fidelity for single-photon states of at least $(93.7 \pm 2.4)\%$. $^{167}Er^{3+}$:YSO at temperatures of approximately 400 mK and a moderate magnetic field is shown to be a promising material for AFC quantum memories. A clear path exists for creating a high-efficiency quantum memory with this material and a nanoscale resonator.

ACKNOWLEDGMENTS

This work was supported by Air Force Office of Scientific Research Young Investigator Award No. FA9550-15-1-0252, Air Force Office of Scientific Research Grant No. FA9550-18-1-0374, and the National Science Foundation (Grant No. EFRI 1741707). I.C. and J.R. acknowledge support from the Natural Sciences and Engineering Research Council of Canada (Grants No. PGSD2-502755-2017 and No. PGSD3-502844-2017). J.G.B. acknowledges support of the American Australian Association's Northrop Grumman Fellowship. N.S. acknowledges funding by the Alliance for Quantum Technologies' Intelligent Quantum Networks and Technologies research program.

APPENDIX A: DEVICE TEMPERATURE

Because of poor thermal conduction at low temperatures in insulating materials such as YSO, and the small cross section of the nanobeam, the device is warmer than its approximately-25-mK surroundings when optical pulses are coupled in. The device temperature is estimated via the $^{167}Er^{3+}$ electron spin temperature [40], which is computed from the ratio between the lower and upper electron spin populations in the optical-ground-state manifold with use of $N_{|\uparrow\rangle}/N_{|\downarrow\rangle} = e^{-\hbar\omega/k_B T}$.

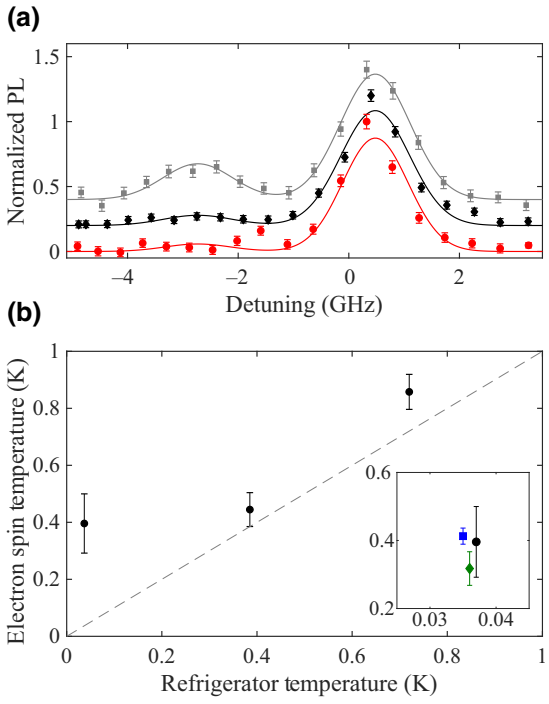

FIG. 5. (a) Photoluminescence (PL) from the nanobeam device as a function of detuning at three refrigerator temperatures: 720 mK (gray squares), 385 mK (black diamonds), and 37 mK (red circles). Detuning is measured from 194 810 ± 0.1 GHz. PL is collected after a 500-μs resonant pulse at 0.3 pW (estimated power in the nanobeam). Background counts are subtracted, and each curve is normalized and offset for clarity. Solid lines are fits to a sum of two Gaussians with equal widths and center frequencies 3.2 GHz apart. The $|\downarrow\rangle$ transition is at the higher frequency. (b) Electron spin temperatures (EST) computed from the PL data in (a) as a function of refrigerator temperature. The dashed gray line indicates where the two temperatures are equal. The inset shows an enlargement of the EST measurement at 37 mK (black circle) and the EST estimated during the T_2 measurement (green diamond) and the 165-ns storage experiment (blue square). To estimate the latter two temperatures, the same pattern of laser pulses as in the actual experiments is sent to the nanobeam, at 0.3 and 0.02 nW, respectively, and PL is collected after the pulses. Error bars are propagated standard deviations from photon counting ($\sqrt{N_{\text{counts}}}$). In all measurements the laser frequency is slowly modulated within each transition to prevent hyperfine hole burning.

Under an applied field of 380 mT, the electron spin in the optical ground state is frozen for any temperature under approximately 500 mK, enabling the long hyperfine lifetimes required for AFC storage. To be sensitive to lower temperatures, measurements of the electron spin population are performed with a lower magnetic field of 110 mT (parallel to the D_1 axis of the crystal), leading to an electron Zeeman splitting of $\omega = 2\pi \times 23$ GHz, where the upper electron spin state has a detectable population down to approximately 250 mK. Because the Zeeman splitting is still considerably greater than the hyperfine splitting, one can consider two electron spin states, $|\downarrow\rangle$ and $|\uparrow\rangle$, each split into eight by the hyperfine interaction. The population in the two electron spin states is measured via the electron-spin-preserving optical transitions from each level. The nanobeam is tuned such that these transitions are both resonant with the cavity, and photoluminescence is collected as a function of frequency, as shown in Fig. 5(a). $N_{|\uparrow\rangle}/N_{|\downarrow\rangle}$ is extracted from the area ratio of the two transitions. Figure 5(b) shows the electron spin temperatures computed from these ratios for different dilution-refrigerator temperatures. The inset in Fig. 5(b) shows the electron spin temperature measured under input power conditions identical to two experiments: 317 ± 49 mK for the T_2 measurement in the nanobeam and 413 ± 24 mK for the 165-ns storage experiment in Fig. 2. Assuming the electron spin is in thermal equilibrium with the device, we estimate the temperature of our device during experiments to be approximately 400 mK.

APPENDIX B: ENSEMBLE COOPERATIVITY

To extract the cooperativity of coupling between the nanobeam resonator and the ensemble of $^{167}Er^{3+}$ ions, each cavity reflection spectrum shown in the inset in Fig. 1(e) is fit with

$$R = \alpha_1 \left| (1-\alpha_f) + \alpha_f e^{i\theta_f} - \frac{i\kappa_{\text{in}}}{\omega - \omega_{\text{cavity}} + i(\kappa/2) + W(\omega, g_{\text{total}}, \Delta_{\text{ions}}, \omega_{\text{ions}})} \right|^2 + \alpha_2, \tag{B1}$$

where α_1 and α_2 are amplitude and background fit parameters, $\alpha_f e^{i\theta_f}$ accounts for Fano interference (both α_f and θ_f are fit parameters), κ is the total cavity energy decay rate, κ_{in} is the coupling rate through the input port, and ω_{cavity} is the cavity resonance frequency. $\kappa = 27.3$ GHz and $\kappa_{\text{in}}/\kappa = 0.21$ are measured from reflection curves where the cavity is detuned from the $^{167}Er^{3+}$ transition. $W(\omega, g_{\text{total}}, \Delta_{\text{ions}}, \omega_{\text{ions}})$ is the rate of absorption of the cavity field by the ensemble of ions, $W \sim \sum_i [g_i^2/(\omega - \omega_i)]$, where g_i is the coupling between one ion and the cavity [16,41]. We approximate the irregular shape of

the inhomogeneously broadened and hyperfine-broadened optical transition as a Gaussian, and use the expression for W from Ref. [41]:

$$W = i\frac{\sqrt{\pi \log 2}\, g_{\text{total}}^2}{\Delta_{\text{ions}}/2}\left[1 - \text{erf}\left(-\frac{i\sqrt{\log 2}(\omega - \omega_{\text{ions}})}{\Delta_{\text{ions}}/2}\right)\right] \times \exp\left[-\log 2\left(\frac{\omega - \omega_{\text{ions}}}{\Delta_{\text{ions}}/2}\right)^2\right], \tag{B2}$$

where Δ_{ions} is the linewidth of the ensemble transition, ω_{ions} its the center, and $g_{\text{total}}^2 = \sum_i g_i^2$. Finally, the ensemble cooperativity is computed with $C = |W(\omega = \omega_{\text{ions}})|/(\kappa/2) = 4\sqrt{\pi \log 2}\, g_{\text{total}}^2/(\kappa \Delta_{\text{ions}})$ [8].

For the case with no initialization, the fit yields $\omega_{\text{cavity}} - \omega_{\text{ions}} = 2\pi \times 2.5$ GHz, $g_{\text{total}} = 2\pi \times 0.79$ GHz, $\Delta_{\text{ions}} = 2\pi \times 1.4$ GHz, and $C = 0.1$.

For the case with initialization, the fit yields $\omega_{\text{cavity}} - \omega_{\text{ions}} = 2\pi \times 1.5$ GHz, $g_{\text{total}} = 2\pi \times 0.70$ GHz, $\Delta_{\text{ions}} = 2\pi \times 0.36$ GHz, and $C = 0.3$.

APPENDIX C: FIDELITY

In the absence of a single-photon source, a lower bound on the storage fidelity of a single-photon input state can be found by the decoy-state-analysis method [27,29]. In this method, a time-bin state ψ with a mean photon number $\bar{n}$ is stored with use of the AFC protocol, and the fidelity $F_\psi^{(\bar{n})}$ of storage is measured as

$$F_\psi^{(\bar{n})} = \frac{N_\psi}{N_\psi + N_{\phi\perp\psi}}, \tag{C1}$$

where N_ψ ($N_{\phi\perp\psi}$) is the number of photons measured in the output time bin corresponding to ψ ($\phi \perp \psi$), where $\phi \perp \psi$ denotes the state orthogonal to ψ. The gain of the output, $Q_\psi^{(\bar{n})}$, is estimated as follows:

$$Q_\psi^{(\bar{n})} = N_\psi + N_{\phi\perp\psi}. \tag{C2}$$

$F_\psi^{(\bar{n})}$ and $Q_\psi^{(\bar{n})}$ are measured for mean photon numbers $\bar{n}_1$ and $\bar{n}_2$, where $\bar{n}_1 < \bar{n}_2$, and $\bar{n}_2 < 1$.

The lower bound on the fidelity of storing a one-photon input state $F_\psi^{(n=1,L)}$ is then computed as follows:

$$F_\psi^{(n=1,L)} = 1 - \frac{E_\psi^{(\bar{n}_1)} Q^{(\bar{n}_1)} \exp \bar{n}_1 - E^{(0)} Y^{(0)}}{Y^{(n=1,L)} \bar{n}_1}, \tag{C3}$$

where

$$E_\psi^{(\bar{n})} = 1 - F_\psi^{(\bar{n})} \tag{C4}$$

is the error rate of storing a state ψ with mean photon number $\bar{n}$, and

$$Y^{(n=1,L)} = \max\left[Y^{(0)}, \frac{\bar{n}_2}{\bar{n}_2\bar{n}_1 - \bar{n}_1^2} \times \left(Q^{(\bar{n}_1)} e^{\bar{n}_1} - Q^{(\bar{n}_2)} e^{\bar{n}_2} \frac{\bar{n}_1^2}{\bar{n}_2^2} - \frac{\bar{n}_2^2 - \bar{n}_1^2}{\bar{n}_2^2} Y^{(0)}\right)\right] \tag{C5}$$

is the lower bound on the detection yield for the storage of a single-photon state (see Ref. [29]). $Y^{(0)} = Q^{(n=0)}$ is the yield when the input state is the vacuum state, and is equal to the dark counts in both output time bins. The superscripts denote the photon number and whether the value is a lower bound (L). $E^{(0)} = E^{(n=0)}$ is the vacuum error rate, which is 0.5 by definition [29].

To obtain an average fidelity bound for all possible time-bin states, the fidelities for storing the time-bin states $|\text{early}\rangle$, $|\text{late}\rangle$, $|+\rangle = (|\text{early}\rangle + |\text{late}\rangle)/\sqrt{2}$, and $|-\rangle = (|\text{early}\rangle - |\text{late}\rangle)/\sqrt{2}$ are measured for input photon numbers $\bar{n}_1 = 0.30$ and $\bar{n}_2 = 0.60$. The input pulses defining the $|\text{early}\rangle$ and the $|\text{late}\rangle$ basis are 60 ns wide and 90 ns apart. A double AFC is used for measurements of all states, with the memory times associated with the two combs being $t_1 = 210$ ns and $t_2 = 300$ ns, such that $t_2 - t_1 = 90$ ns. Of the three output time bins [see the inset in Fig. 4(b)], the first and third are used to measure F_{early} and F_{late}, while the second time bin is used to measure F_+ and F_-.

Following Eq. (C3), $F_+^{(n=1,L)}$ is computed as follows:

$$F_+^{(n=1,L)} = 1 - \frac{E_+^{(\bar{n}_1)} Q_{+/-}^{(\bar{n}_1)} \exp \bar{n}_1 - E^{(0)} Y_{+/-}^{(0)}}{Y_{+/-}^{(n=1,L)} \bar{n}_1}, \tag{C6}$$

with similar equations for the other three states. $Q_{+/-}^{(\bar{n}_1)}$, $Y_{+/-}^{(0)}$, and $Y_{+/-}^{(n=1,L)}$ are averaged over the $|+\rangle$ and $|-\rangle$ fidelity measurements.

The lower bound on the fidelity of storing an arbitrary single-photon state, $F_{\text{average}}^{(n=1,L)} = (93.7 \pm 2.4)\%$, is then computed as follows:

$$F_{\text{average}}^{(n=1,L)} = \frac{1}{3}\left(\frac{F_{\text{early}}^{(n=1,L)} + F_{\text{late}}^{(n=1,L)}}{2}\right) + \frac{2}{3}\left(\frac{F_+^{(n=1,L)} + F_-^{(n=1,L)}}{2}\right). \tag{C7}$$

Table I summarizes the measured fidelity values for storing weak coherent states. The uncertainties are calculated using $\sqrt{N_{\text{photon}}}$ standard deviation on all N_ψ values due to Poissonian statistics of photon counting and the uncertainty, estimated to be 15%, of the mean input photon numbers, $\bar{n}$.

TABLE I. Measured storage fidelities in the nanobeam device.

Input photon number	$\frac{1}{2}\left(F^{(\bar{n})}_{\text{early}} + F^{(\bar{n})}_{\text{late}}\right)$	$\frac{1}{2}\left(F^{(\bar{n})}_{+} + F^{(\bar{n})}_{-}\right)$
$\bar{n} = 0.60 \pm 0.09$	$(89.04 \pm 1.34)\%$	$(91.90 \pm 1.32)\%$
$\bar{n} = 0.30 \pm 0.05$	$(82.59 \pm 1.80)\%$	$(90.75 \pm 1.84)\%$
$n = 0$	50%	50%

APPENDIX D: STORAGE EFFICIENCY

The efficiency of AFC storage in a cavity is given by [16,21,23]

$$\eta_{\text{AFC}} = \left(\frac{4\kappa_{\text{in}}\,\Gamma_{\text{comb}}}{(\kappa_{\text{total}} + \Gamma_{\text{comb}} + \Gamma_{\text{bg}})^2}\right)^2 \eta_d, \tag{D1}$$

where κ_{in} is the rate of cavity coupling through the input port, κ_{total} is the total energy decay rate of the cavity, $\eta_d = \exp\left[-\pi^2/(2\log 2(\Delta/\gamma)^2)\right]$ accounts for dephasing due to the finite width of the comb teeth [11], and Γ_{comb} and Γ_{bg} are the rates of absorption of the cavity field by the ensemble of ions in the comb and the background, respectively. Background ions are those ions remaining after optical pumping, with transition frequencies where transparency is desired (i.e., between the teeth of the comb). Nonzero Γ_{bg} results from limitations in spectral hole burning. With use of η_{spectral}, the fractional optical depth of a spectral hole, Δ, the intertooth spacing, and γ, the width of one comb tooth, Γ_{comb} and Γ_{bg} can be estimated as follows:

$$\Gamma_{\text{comb}} \approx \eta_{\text{spectral}}\frac{\gamma}{\Delta}\Gamma_{\text{ions}}, \tag{D2}$$

$$\Gamma_{\text{bg}} = (1 - \eta_{\text{spectral}})\Gamma_{\text{ions}}, \tag{D3}$$

where $\Gamma_{\text{ions}} = |W(\omega = \omega_{\text{ions}})| = \sqrt{\pi\log 2}\,g^2_{\text{total}}/(\Delta_{\text{ions}}/2)$ is the rate of absorption of the cavity field by the ensemble of ions before comb preparation (see Appendix B).

We can define an effective AFC cooperativity, C':

$$C' = \frac{\Gamma_{\text{comb}} + \Gamma_{\text{bg}}}{\kappa_{\text{total}}/2} = \left[\eta_{\text{spectral}}\frac{\gamma}{\Delta} + (1 - \eta_{\text{spectral}})\right] C. \tag{D4}$$

Rewriting Eq. (D1) gives rise to the following expression for the AFC storage efficiency:

$$\eta_{\text{AFC}} = \left(\frac{1}{(\Delta/\gamma)(\frac{1}{\eta_{\text{spectral}}} - 1) + 1}\,\frac{\kappa_{\text{in}}}{\kappa_{\text{total}}}\,\frac{4C'}{(1 + C')^2}\right)^2 \eta_d, \tag{D5}$$

The efficiency is maximized when $C' \to 1$.

The predicted efficiency of storage in the nanobeam is $\eta_{\text{AFC}} = 0.17\%$, which is found with $C = 0.3$, $\kappa_{\text{in}}/\kappa_{\text{total}} = 0.21$, and a measured finesse of $\Delta/\gamma = 2.1$ and by our assuming a perfect comb, $\eta_{\text{spectral}} = 1$. This is similar to the measured value of 0.20% for a storage time of 165 ns.

To increase the memory efficiency, the ensemble cooperativity and the ratio $\kappa_{\text{in}}/\kappa_{\text{total}}$ must be increased. We first consider increasing the concentration and improvement of initialization of $^{167}Er^{3+}$ ions, keeping the nanophotonic resonator the same. By increasing the ion concentration to 200 ppm (assuming no significant increase in inhomogeneous linewidth), and using the level of initialization achieved in the work reported in Ref. [12] (95%), we expect a cooperativity of $C = 3$. With the measured $\kappa_{\text{in}}/\kappa_{\text{total}} = 0.21$ and a comb finesse of $\Delta/\gamma = 3$, ($C' = 0.73$), the predicted efficiency is 3%. This memory efficiency is mainly limited by the loss from the cavity, the term $(\kappa_{\text{in}}/\kappa_{\text{total}})^2$ in Eq. (D5). The total cavity loss rate is $\kappa_{\text{total}} = \kappa_{\text{in}} + \kappa_i$, where κ_i is the intrinsic loss, including losses from absorption, scattering, and the imperfect reflectivity of the second mirror.

A memory efficiency greater than 90% can be achieved if the intrinsic quality factor of the resonator is increased from its current value of $Q_i \sim 9000$ to 2×10^6 and $\kappa_{\text{in}}/\kappa_{\text{total}}$ is increased to 0.97. The latter can be accomplished with a resonator with one mirror having relatively low reflectivity, and with minimal losses through other channels (transmission through the second mirror, scattering, absorption). This calculation assumes the same material as described above (200 ppm, ideal initialization into one hyperfine state) and a comb finesse of 13. It also accounts for a decrease by a factor of approximately 3 in the cooperativity that results from switching to a hybrid silicon-YSO platform where the evanescent cavity-ion coupling is weaker. With this storage efficiency, the memory would match the performance of an optical fiber (0.15 dB/km) at $t_{\text{storage}} = 10\ \mu$s [39].

For a finesse of $f = 13$ and a storage time of 10 μs, the corresponding comb tooth width is $\gamma = \Delta/f = 8$ kHz, which is too narrow for $^{167}Er^{3+}$:YSO, where effective linewidths are limited to 1 MHz by superhyperfine coupling. However, memory times longer than 10 μs can be achieved with a nanoresonator in this material by use of the spin-wave AFC [11].

[1] H. J. Kimble, The quantum internet, Nature **453**, 1023 (2008).
[2] K. Heshami, D. G. England, P. C. Humphreys, P. J. Bustard, V. M. Acosta, J. Nunn, and B. J. Sussman, Quantum memories: Emerging applications and recent advances, J. Mod. Opt. **63**, 2005 (2016).
[3] H.-J. Briegel, W. Dür, J. I. Cirac, and P. Zoller, Quantum Repeaters: The Role of Imperfect Local Operations in Quantum Communication, Phys. Rev. Lett. **81**, 5932 (1998).

[4] P. Kok, W. J. Munro, K. Nemoto, T. C. Ralph, J. P. Dowling, and G. J. Milburn, Linear optical quantum computing with photonic qubits, Rev. Mod. Phys. **79**, 135 (2007).

[5] C. Monroe, R. Raussendorf, A. Ruthven, K. R. Brown, P. Maunz, L.-M. Duan, and J. Kim, Large-scale modular quantum-computer architecture with atomic memory and photonic interconnects, Phys. Rev. A **89**, 022317 (2014).

[6] C. Thiel, T. Böttger, and R. Cone, Rare-earth-doped materials for applications in quantum information storage and signal processing, J. Lumin. **131**, 353 (2011).

[7] M. Zhong, M. P. Hedges, R. L. Ahlefeldt, J. G. Bartholomew, S. E. Beavan, S. M. Wittig, J. J. Longdell, and M. J. Sellars, Optically addressable nuclear spins in a solid with a six-hour coherence time, Nature **517**, 177 (2015).

[8] E. Miyazono, I. Craiciu, A. Arbabi, T. Zhong, and A. Faraon, Coupling erbium dopants in yttrium orthosilicate to silicon photonic resonators and waveguides, Opt. Express **25**, 2863 (2017).

[9] E. Saglamyurek, J. Jin, V. B. Verma, M. D. Shaw, F. Marsili, S. W. Nam, D. Oblak, and W. Tittel, Quantum storage of entangled telecom-wavelength photons in an erbium-doped optical fibre, Nat. Photonics **9**, 83 (2015).

[10] M. F. Askarani, M. G. Puigibert, T. Lutz, V. B. Verma, M. D. Shaw, S. W. Nam, N. Sinclair, D. Oblak, and W. Tittel, Storage and Reemission of Heralded Telecommunication-Wavelength Photons using a Crystal Waveguide, Phys. Rev. Appl. **11**, 054056 (2019).

[11] M. Afzelius, C. Simon, H. de Riedmatten, and N. Gisin, Multimode quantum memory based on atomic frequency combs, Phys. Rev. A **79**, 052329 (2009).

[12] M. Rančić, M. P. Hedges, R. L. Ahlefeldt, and M. J. Sellars, Coherence time of over a second in a telecom-compatible quantum memory storage material, Nat. Phys. **14**, 50 (2018).

[13] B. Lauritzen, J. Minář, H. de Riedmatten, M. Afzelius, N. Sangouard, C. Simon, and N. Gisin, Telecommunication-wavelength Solid-State Memory at the Single Photon Level, Phys. Rev. Lett. **104**, 080502 (2010).

[14] B. Lauritzen, J. Minář, H. de Riedmatten, M. Afzelius, and N. Gisin, Approaches for a quantum memory at telecommunication wavelengths, Phys. Rev. A **83**, 012318 (2011).

[15] J. Dajczgewand, J.-L. L. Gouët, A. Louchet-Chauvet, and T. Chanelière, Large efficiency at telecom wavelength for optical quantum memories, Opt. Lett. **39**, 2711 (2014).

[16] M. Afzelius and C. Simon, Impedance-matched cavity quantum memory, Phys. Rev. A **82**, 022310 (2010).

[17] T. Zhong, J. Rochman, J. M. Kindem, E. Miyazono, and A. Faraon, High quality factor nanophotonic resonators in bulk rare-earth doped crystals, Opt. Express **24**, 536 (2016).

[18] R. W. P. Drever, J. L. Hall, F. V. Kowalski, J. Hough, G. M. Ford, A. J. Munley, and H. Ward, Laser phase and frequency stabilization using an optical resonator, Appl. Phys. B **31**, 97 (1983).

[19] I. D. Abella, N. A. Kurnit, and S. R. Hartmann, Photon echoes, Phys. Rev. **141**, 391 (1966).

[20] T. Zhong, J. M. Kindem, E. Miyazono, and A. Faraon, Nanophotonic coherent light-matter interfaces based on rare-earth-doped crystals, Nat. Commun. **6**, 8206 (2015).

[21] T. Zhong, J. M. Kindem, J. G. Bartholomew, J. Rochman, I. Craiciu, E. Miyazono, M. Bettinelli, E. Cavalli, V. Verma, S. W. Nam, F. Marsili, M. D. Shaw, A. D. Beyer, and A. Faraon, Nanophotonic rare-earth quantum memory with optically controlled retrieval, Science **357**, 1392 (2017).

[22] S. Mosor, J. Hendrickson, B. C. Richards, J. Sweet, G. Khitrova, H. M. Gibbs, T. Yoshie, A. Scherer, O. B. Shchekin, and D. G. Deppe, Scanning a Photonic Crystal Slab Nanocavity by Condensation of Xenon, Appl. Phys. Lett. **87**, 141105 (2005).

[23] S. A. Moiseev, S. N. Andrianov, and F. F. Gubaidullin, Efficient multimode quantum memory based on photon echo in an optimal qed cavity, Phys. Rev. A **82**, 022311 (2010).

[24] H. de Riedmatten, M. Afzelius, M. U. Staudt, C. Simon, and N. Gisin, A solid-state light-matter interface at the single-photon level, Nature **456**, 773 (2008).

[25] O. Guillot-Noël, H. Vezin, P. Goldner, F. Beaudoux, J. Vincent, J. Lejay, and I. Lorgeré, Direct observation of rare-earth-host interactions in Er : Y_2SiO_5, Phys. Rev. B **76**, 180408 (2007).

[26] B. Car, L. Veissier, A. Louchet-Chauvet, J.-L. Le Gouët, and T. Chanelière, Selective Optical Addressing of Nuclear Spins through Superhyperfine Interaction in Rare-earth Dopedsolids, Phys. Rev. Lett. **120**, 197401 (2018).

[27] N. Sinclair, E. Saglamyurek, H. Mallahzadeh, J. A. Slater, M. George, R. Ricken, M. P. Hedges, D. Oblak, C. Simon, W. Sohler, and W. Tittel, Spectral Multiplexing for Scalable Quantum Photonics Using an Atomic Frequency Comb Quantum Memory and Feed-forward Control, Phys. Rev. Lett. **113**, 053603 (2014).

[28] S. Welinski, C. W. Thiel, J. Dajczgewand, A. Ferrier, R. L. Cone, R. M. Macfarlane, T. Chanelière, A. Louchet-Chauvet, and P. Goldner, Effects of disorder on optical and electron spin linewidths in Er^{3+}, Sc^{3+} : Y_2SiO_5, Opt. Mater. **63**, 69 (2017).

[29] X. Ma, B. Qi, Y. Zhao, and H.-K. Lo, Practical decoy state for quantum key distribution, Phys. Rev. A **72**, 012326 (2005).

[30] S. A. Zargaleh, S. Hameau, B. Eble, F. Margaillan, H. J. von Bardeleben, J. L. Cantin, and W. Gao, Nitrogen vacancy center in cubic silicon carbide: A promising qubit in the 1.5 μm spectral range for photonic quantum networks, Phys. Rev. B **98**, 165203 (2018).

[31] J. Wang, Y. Zhou, Z. Wang, A. Rasmita, J. Yang, X. Li, H. J. von Bardeleben, and W. Gao, Bright room temperature single photon source at telecom range in cubic silicon carbide, Nat. Commun. **9**, 4106 (2018).

[32] D. Rieländer, A. Lenhard, M. Mazzera, and H. de Riedmatten, Cavity enhanced telecom heralded single photons for spin-wave solid state quantum memories, New J. Phys. **18**, 123013 (2016).

[33] A. M. Dibos, M. Raha, C. M. Phenicie, and J. D. Thompson, Atomic Source of Single Photons in the Telecom Band, Phys. Rev. Lett. **120**, 243601 (2018).

[34] M. Paul, F. Olbrich, J. Hschele, S. Schreier, J. Kettler, S. L. Portalupi, M. Jetter, and P. Michler, Single-photon emission at 1.55 μm from MOVPE-grown inAs quantum dots on InGaAs/GaAs metamorphic buffers, Appl. Phys. Lett. **111**, 033102 (2017).

[35] S. Atzeni, A. S. Rab, G. Corrielli, E. Polino, M. Valeri, P. Mataloni, N. Spagnolo, A. Crespi, F. Sciarrino, and R. Osellame, Integrated sources of entangled photons at the telecom wavelength in femtosecond-laser-written circuits, Optica **5**, 311 (2018).

[36] K. Niizeki, K. Ikeda, M. Zheng, X. Xie, K. Okamura, N. Takei, N. Namekata, S. Inoue, H. Kosaka, and T. Horikiri, Ultrabright narrow-band telecom two-photon source for long-distance quantumcommunication, Applied Physics Express **11**, 042801 (2018).

[37] Y. Zhou, Z. Wang, A. Rasmita, S. Kim, A. Berhane, Z. Bodrog, G. Adamo, A. Gali, I. Aharonovich, and W.-B. Gao, Room temperature solid-state quantum emitters in the telecom range, Sci. Adv. **4**, 1 (2018).

[38] A. Dréau, A. Tchebotareva, A. E. Mahdaoui, C. Bonato, and R. Hanson, Quantum Frequency Conversion of Single Photons from a Nitrogen-vacancy Center in Diamond to Telecommunication Wavelengths, Phys. Rev. Appl. **9**, 064031 (2018).

[39] Y.-W. Cho, G. T. Campbell, J. L. Everett, J. Bernu, D. B. Higginbottom, M. T. Cao, J. Geng, N. P. Robins, P. K. Lam, and B. C. Buchler, Highly efficient optical quantum memory with long coherence time in cold atoms, Optica **3**, 100 (2016).

[40] N. Kukharchyk, D. Sholokhov, O. Morozov, S. L. Korableva, A. A. Kalachev, and P. A. Bushev, Optical coherence of ^{166}Er:^{7}LiYF$_4$ crystal below 1 k, New J. Phys. **20**, 023044 (2018).

[41] I. Diniz, S. Portolan, R. Ferreira, J. M. Gérard, P. Bertet, and A. Auffèves, Strongly coupling a cavity to inhomogeneous ensembles of emitters: Potential for long-lived solid-state quantum memories, Phys. Rev. A **84**, 063810 (2011).